1
2
3
4
5
6
7
8
9
10
11
12
13
14
15
16
17
18
19
20
21
22
23
24
25
26
27
28
29
30
31
32
33
34
35
36
37
38
39
40
41
42
43
44
45
46
47
48
49
50
51
52
53
54
55
56
57
58
59
60
61
62
63
64
65

The Use of a Swept Frequency Alternating Current Potential Difference Method for Identifying Local Geometric Features within Prismatic Conductors

Yuqian Si, Thomas M Buss, James P Rouse, and Christopher J Hyde

University of Nottingham, University Park, Nottingham NG7 2RD, UK

Abstract

Potential difference methods are widely accepted as means to detect and monitor cracks in safety critical components. This paper investigates the capability of the potential difference method that uses a swept frequency alternating current excitation (i.e. skin effect with varying current penetration depths) in identifying conductor shapes and features through experiments and finite element analysis. The study focused on samples with the size of 55 mm $\times$ 100 mm^2 and surface features with opening widths vary from 11% to 42% to the sample size. The method has been investigated by finite element analysis with the capability to distinguish cross-sectional shapes of non-magnetic conductors due to prominent current crowding on surfaces, in which the potential differences measured from a SS316 conductor of triangular cross-sectional shape are higher to those of a circular shape by 77% at 300 kHz. The detection capability of the method has also be confirmed, which is attributed to the impact of feature openings on skin effect. At 50 kHz, potential differences measured across features with the same cross-sectional area of 9 mm^2 on EN1A samples rise by 130% as the opening width increase from 11% to 42% to the sample size.

Introduction

The detection and monitoring of cracks for damaged components has been recognised as a key problem within several sectors including energy, aerospace, and automotive. Non-destructive testing (NDT) techniques, which provide accurate characterisation of defects without causing additional damage to components, have been widely developed and employed to monitor crack growth. Of the various NDT techniques, potential difference (PD) methods have gained wide acceptance due to ease of operation [1–7], ability of providing accurate and continuous predictions [2–4, 6, 8, 9], and applicability in various environments such as corrosion [10–12], high temperature [13–15], etc. PD methods are based on the principle of the resistance of a flawed conductor (i.e. containing a crack) increase as the crack propagates. By applying a current to the conductor, PDs measured across the crack are used to identify the crack depth. In conventional applications of PD methods, the length of the tested crack is usually inferred from PDs measured across it by an established calibration curve. Calibration curves of various cracks have been determined by the use of analytical [16–18], numerical [8, 19, 20], direct [5, 14, 19]

and analogue [2–5,17] experimental methods in the past decades. Comprehensive review including recent and early works of PD methods can be found in [21]. Depending on the type of operating current, PD methods can be characterised as direct current (DC) or alternating current (AC) PD. In DCPD, the whole cross-sectional of the conductor carries the uniform current distribution. While in ACPD, the eddy current is induced by the varying magnetic filed which is generated by the AC. The current in ACPD is counteracted by the induced eddy current thus forced to flow within a thin region beneath the sample surface, i.e. the skin effect. The depth of current penetration, known as the skin depth (δ), can be approximated by Equation (1) [22, 23].

$$\delta = \sqrt{\frac{2}{\mu\sigma\omega}} \tag{1}$$

where μ and σ are the conductor's magnetic permeability and electrical conductivity, respectively, and ω is the excitation frequency.

By taking the advantage of skin effect, AC around a surface crack is often suggested to have the ability to delineate the crack edge (or part of the edge). Therefore, ACPD methods are expected to be capable of identifying cracks, especially cracks of the same cross-sectional areas and various shapes beyond the capability of DCPD. Venkatsubramanian and Unvala [24] have applied multi-frequency ACPD methods to monitor crack growth of wedge opening loaded specimen and gave a single calibration curve at 150 Hz, 1 kHz, 10 kHz. Nakai and Wei [25] have observed different linear calibration curves of cracks in single edge notched (SEN) specimens at multiple frequencies. The linear slopes of calibration curves decreased as the frequency reducing from 940 Hz to 93 Hz. Hwang [26] and Tiku et al [27] have obtained second-order polynomial calibration curves of SEN specimens at various frequencies (17, 127, and 203 kHz in [26] and 30, 90, 120 kHz in [27]). In addition to establish calibration curves of standard surface cracks, multi-frequency ACPD methods have been applied to identify locations and sizes of internal and bottom cracks based on numerical approaches [28–30]. Compared with the ACPD methods sampled by stepped frequencies, swept frequency ACPD methods can be used to measure plenty of information for crack identifying with much shorter time. It is applicable to some fatigue conditions in which cracks propagate rapidly. Therefore, by injecting swept frequency AC into cracked conductors, the AC distributions are disturbed by the existence of cracks especially near the surfaces due to the skin effect. PDs measured from proper positions around the features with sufficient accuracy over a wide range of swept frequency are expected to reflect correlations with the crack shapes. In this work, the potential of swept frequency ACPD methods in monitoring cracks were investigated. The experimental system developed by Buss et al [31] has been utilised to supply AC with rapidly varying frequency from 10 Hz to 300 kHz and measure signals in the time interval of 2 secs.

The objectives of the work are focused on investigating the capability of the swept ACPD method in two aspects, firstly to detect the shapes of plain conductors with the same cross-sectional area, secondly to identify cracks/features with different opening geometries and depths. The first objective was designed for model validation including the experimental and data processing procedures, and especially the capability and sensitivity of the swept frequency ACPD method. Several conductive samples were manufactured with the same gauge size of 55 mm × 100 mm² for the ACPD experiments, including four plain bars in 316 stainless steel (SS316) of different cross-sectional shapes and five featured bars in EN1A mild steel (EN1A) containing various features. Swept ACPD

signals were measured from the samples based on a uniform probe configuration, and then processed by a data processing script in MATLAB. Finite element (FE) models of all samples have been created via ANSYS to simulate the current distributions generated within around the samples in ACPD experiments. FE results of PD were compared with experimental results, and furthermore, field solutions were used to understand the principle of the detection capability.

Methodology

Experimental Procedures and Data Processing

The experimental samples were divided into 3 cases to sequentially investigate the detection capability of the swept ACPD method in identifying

- cross-sectional shapes of plain conductors (Case 1);
- features with distinct geometries like a narrow drill and a wide notch (Case 2);
- features with the same cross-sectional area (Case 3).

Sample information are summarised in Table 1. Features manufactured for Cases 2-3 are shown in Figure 1. Case 2 consists of three features with different geometries, which are the cylindrical drill with a narrow curved opening (H), the wide notch with a wide rectangular opening (N6, as shown in Figure 2), and a combination of the two (NH). Following this, two other features were produced to have the same thickness and cross-sectional area (of 9 mm^2 as shadowed in Figure 1) with the N6 feature. These three features constituent Case 3 and are named based on their widths to be N6, N3, and N1.5.

Sample	Material	Sample Shape	Feature Type
Case 1			
1-1		Circular	
1-2	SS316	Hexagonal	Plain
1-3		Square	
1-4		Triangular	
Case 2			
2-1			H
2-2	EN1A	Square	N6
2-3			NH
Case 3			
3-1			N6
3-2	EN1A	Square	N3
3-3			N1.5

Table 1: Information of the experimental samples.

A swept sinusoidal wave of AC that sampled frequencies from 10 Hz to 300 kHz in 2 secs with a constant amplitude was supplied in experiments. The amplitude was determined to be 3 A in all cases, which supplies measurable outputs without causing undesired localised heating. The swept AC was generated using LabVIEW by following Equation (2) [31].

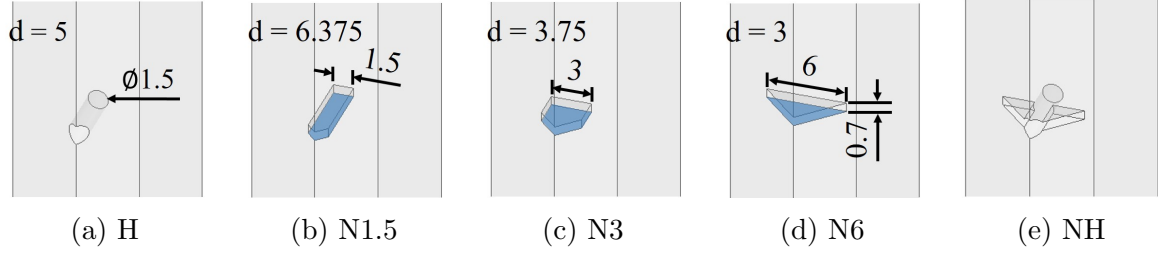$$I = 3\sin\left(2.718^{5t}\omega\right) \tag{2}$$

Figure 1: Features on the EN1A samples in Cases 2-3. d refers to the depth into the sample. All dimensions are in mm.

where t is the time. The AC injection wires and PD measurement probes were welded on the uniform positions on all samples, as shown in Figure 2. The input AC was injected to the samples through a pair of silver steel wires close to the edges and near to the end faces. The wires were bent and then connected to the current input lead by a screw terminal block and to the samples by spot welding. Another pair of thin electric probes for measuring PDs were welded close to the same edges with current injections and around the midpoints of the sample length with a distance of 2 mm. A die-cast aluminium box was used to shield the wires and the connector block from electromagnetic (EM) interference. The box was electrically insulated from the samples by means of a thin polymer tape. A shielded instrument wire was used to continue the shielding to the amplifier. This enabled nearly the whole length of the measurement wires to be shielded from EM pickup.
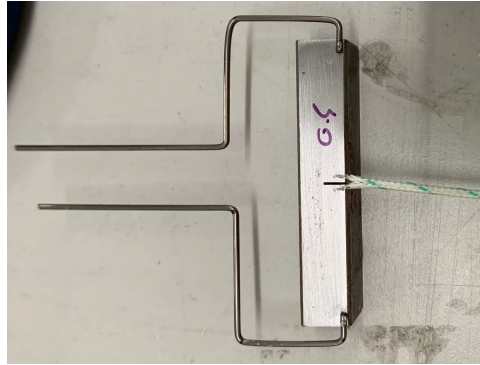

Figure 2: The configuration of injection and measurement wires on experimental samples.

Figure 3 shows the equipment and procedures of the ACPD experiments. The input of swept AC was outputted through an NI-PXIe-6124 input/output module, then fed into a bespoke amplifier supplied by Fylde Electronics, and injected into the samples through the pair of bent injection wires (as described above). PDs were measured from the sample center and fed back into the same PXI unit. Since PDs were smaller than 0.05 mV at low frequencies, the signals were amplified 1000 times using a Fylde FE-H793-TA before the PXI unit. The signals were read back at a sampling frequency (f_s) of 4 MHz.

Before measuring the nine samples in Cases 1-3, the ACPD experiments outlined here were conducted on several conductors and circuits with known impedance behaviours (e.g. an isolated copper rod and resistor-inductor combined circuits) to establish the data processing. For example, processed impedance ($|Z|$ and θ_Z) of the copper rod of 1 m $\times$ 4 mm were compared with theoretical solutions based on the Bessel Function
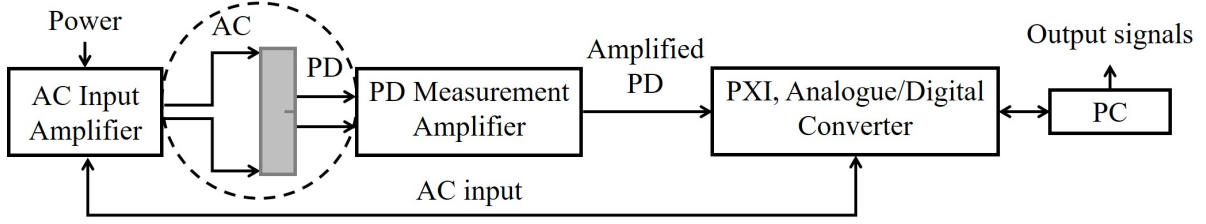
Figure 3: Schematics of the equipment and process of the ACPD experiments.

Method [22, 32–34] and manually measured results, giving good agreement with average differences smaller than 3% from 10 Hz to 300 kHz.

Raw signals in the time domain were processed to calculate frequency-related quantities (e.g. amplitudes and phase angles of signal periods) by the use of a MATLAB script. For example, raw data and processed results in the form of impedance for the plain circular SS316 sample are presented in Figure 4. The script consists of three steps in which AC and PD (i.e. current and voltage) signals are identified and separated into individual periods successively, and then modulus and phase of impedance are computed based on interpreted results of AC and PD. The main challenge is to recognise and separate signals, which are continuously distributed in the time interval, into individual periods at discrete frequencies. This is solved in the script by applying Constant Slope Ratio Method (CSRM) in the first step of current identification. CSRM is devised based on the principle that slopes between any two points on the same ascending or declining segment of the sinusoidal wave are almost identical and distinctly different to the slopes for the next (declining or ascending) segment. The ratio between the two slopes of two adjacent segments are constant at all frequencies provided that all segments are in the same magnitude, e.g. containing signals between the same range of $\pm\frac{1}{3}$ of the amplitude ($|I|$). Therefore, a constant slope ratio can be used to separate signals into segments over the whole time interval, and thus AC signals can be continuously identified with discrete associated frequencies. Furthermore, the magnitude of segments is adjusted with the increasing frequencies to adapt different situations due to the constant f_s. A smaller magnitude (e.g. $\pm\frac{1}{3}|I|$) is used for low frequencies without effective skin effect to exclude excess signals and reduce the computing time; while a larger value (e.g. $|I|$) is applied for high frequencies to cover enough signals and retain the precision. Then in the second step, PD signals are identified by a series of conditional statements based on the symmetry of the sinusoidal wave to find out the corresponding PD periods leading the AC periods at the same frequency (noting that the voltage leads current with a load of inductive nature in the circuit).

Processed results were compared with manually measured results for all experiments to validate the data processing in Cases 1-3. For example, processed and manually measured results of the circular SS316 sample is shown in Figure 4b. The average difference between two types of results of $|Z|$ is 7%, which is mainly due to error signals and small magnitudes of results at frequencies lower than 10 kHz. By excluding the low-frequency comparisons, average differences of $|Z|$ and θ_Z in Figure 4b are of 1.4% and 2.4% respectively. It will be demonstrated later that electric fields generated on the samples are uneven and concentrate near to edges and features. This suggests that ACPD results measured from the uniform positions on the sample surfaces are not representative of the whole field or to be used to calculate 'real impedance' of the conductive body between measuring points. The analysis of ACPD results for samples, especially features samples

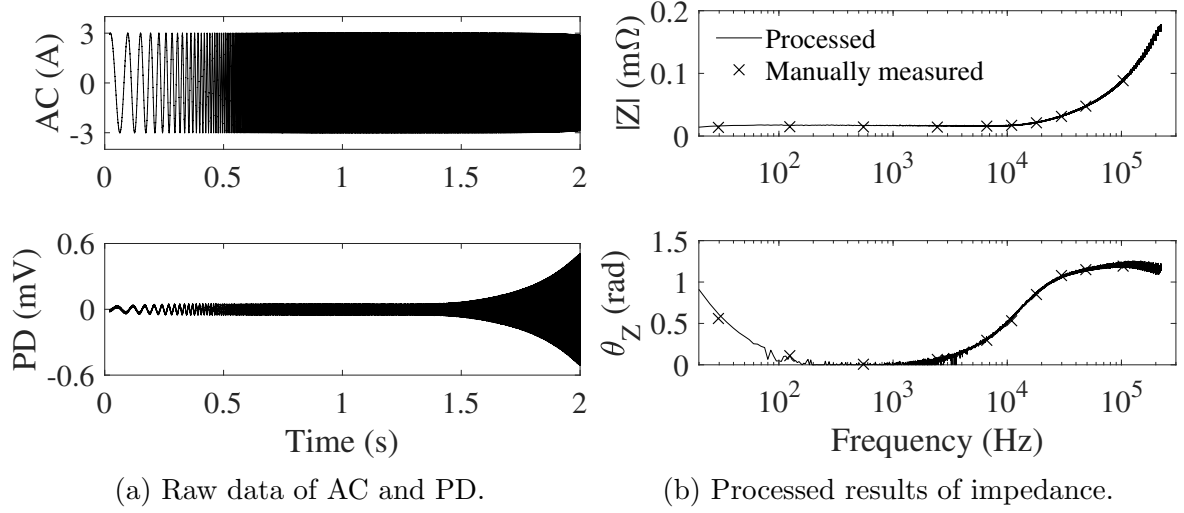(a) Raw data of AC and PD.

(b) Processed results of impedance.

Figure 4: Raw and processed results of the plain circular sample in SS316.

in Cases 2-3, will be focused on PDs rather than impedance. Average differences between processed and manually measured results of PD for all the nine samples in Cases 1-3 are within 8% including low-frequency comparisons.

Finite Element Analysis

Electric fields and current distributions generated with and around the samples in the swept ACPD experiments were simulated by FEA via the Eddy Current solver in the Maxwell 3D module within the ANSYS Electronics Desktop. During the preparatory stage before modelling the experimental samples, mesh refinement studies were conducted for SS316 and EN1A models, separately. Furthermore, the effect of welding uncertainties (i.e. welding positions and lengths) of current injection wires were investigated by creating several pilot models that cover a wide range of possible uncertainties. It was concluded that different welding positions of current wires cause various impact on electric fields within a short distance of about 5 mm near the ends of both SS316 and EN1A samples and produce negligible influence on measurements at the center, e.g. differences in current fields approximated by pilot models for SS316 samples at 100 kHz are within 1%. Therefore, the welding uncertainties of current wires are excluded, and moreover, the current wires can be removed from models to improve the simulation efficiency. Due to the ferromagnetism of EN1A, numerous elements are required in EN1A models to approximate thin skin depths. For example, a model that includes half of an EN1A sample and a current wire generates about 2.5M tetrahedral elements to reach a convergence of 1% at 10 Hz (with $\delta = 0.34$ mm). To reduce the model sizes and save simulation time, partial models which only contain the middle parts of 10 mm around the center of the samples were created. The partial models were further simplified by applying symmetry boundary conditions on symmetry planes by defining a normal magnetic field intensity. The feasibility of partial and symmetric (PS) modelling was validated by comparing between approximated results of PS models to those of complete models consisting of full samples and current wires. For example, Figure 5 demonstrates current fields given by a complete and PS model for the square SS316 sample.

The main tasks of the post processing are to measure PDs over conductive paths for comparing with experimental results and approximate current distributions for further
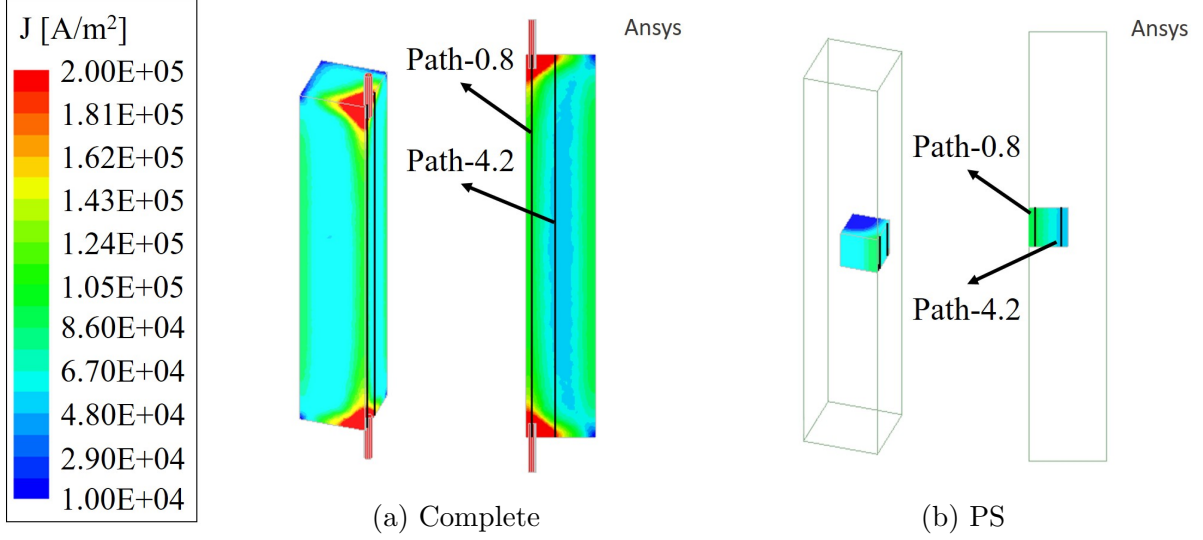
6

Figure 5: Current fields approximated by the complete model and PS model of the square SS316 sample at 100 kHz.

analysing. The output of fields is straightforward in ANSYS Maxwell. For the task of measuring PDs, the conductive paths measured in experiments are defined on the models first, then the PDs over paths are measured by integrating tangential components of electric fields along the paths. It was measured that approximate 1 mm of the measurement probes were welded on the samples to ensure robust connection, giving a possible measurement region from 0.3 mm to 1.3 mm to the edges (see in Figure 2). Moreover, the measurement distances in vertical are not exactly 2 mm on all samples but varied from 1.5 to 3 mm. Due to such unavoidable uncertainties in welding the PD measurement probes, it is unclear over which of the paths were measured in experiments. The measurement uncertainties were simulated by measuring PDs from multiple paths, as shown in Figure 6. The number in the path name refers to the distance to the sample edge. The middle path of Path-0.8 was created to measure PDs in 2 mm of distance (1 mm on PS models) as the nominal FE approximations. Two auxiliary paths of Path-0.5 and Path-1.1 were defined to produce error bars I which contains ±0.3 mm offset in measurement locations. Another two paths of Path-Dis-1.5 and Path-Dis-3, which are at the same location as Path-0.8 but have different vertical lengths of 0.75 mm and 1.5 mm on PS models, were created for error bars II to cover uncertainties in measurement distances. Detailed information of the conductive paths are presented in Table 2.

	Path	Measurement Location	Measurement Distance
Nominal	Path-0.8	0.8	2
Error bar I	Path-0.5	0.5	2
	Path-1.1	1.1	
Error bar II	Path-Dis-1.5	0.8	1.5
	Path-Dis-3		3

Table 2: Information of error bars and conductive paths on FE model.
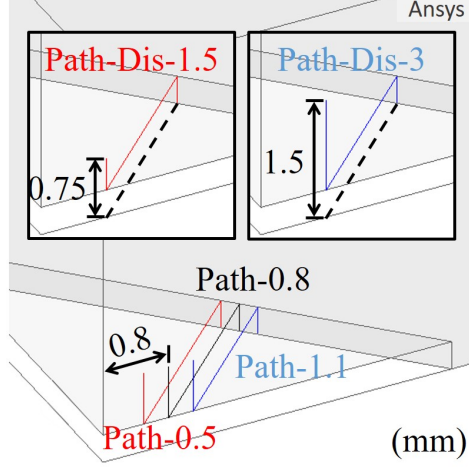
7

Figure 6: The nominal simulation path (Path-0.8) and auxiliary paths for error bars on the PS N6-featured model.

Analytical Solutions of Internal Impedance

Internal impedance (Z_{int}) and AC resistance (R_{ac}) of conductors of uniform cross-sectional shapes and infinitely long have been widely solved [35–40] (e.g. the Bessel Function method for cylindrical bars). With longitudinal current fields and uniform cross-sectional shapes, the measurement part at the center of the SS316 samples may be assumed as a section of an infinitely length conductor. Z_{int} (or R_{ac}) per unit length of the four SS316 samples can be calculated by using available analytical methodology. Analytical solutions of Z_{int} were compared with FE results to validate the precision of FEA and used to roughly approximate PDs.

Silvester [36] and Antonini [37] have put forward a theory to solve Z_{int} of rectangular conductor based on an integral equation of current over the cross-section. A brief introduction of the theory is presented below. In this method, the cross-section is divided into finite parallel subsections with areas small enough so that the current distributions and resistance of subsections are assumed to be uniform within subsections. Mutual and self induction occurring around all individual subsections are used to approximate the total current field over the conductor cross-section, see in Equation (3).

$$J\left(x,y\right) = -\frac{j\omega\mu\sigma}{2\pi} \int \int J\left(\xi,\eta\right) \log \sqrt{\left(x-\xi\right)^2 + \left(y-\eta\right)^2} d\xi d\eta + J_{imp} \quad (3)$$

where J_{imp} is impressed current density. By assuming all subsections are in square with the same area of $a_s{}^2$, Equation (3) may be applied to a subsection approximately to give Equation (4).

$$J_p = -\frac{j\omega\mu\sigma}{2\pi} a_s{}^2 \sum_q^N J_q \log \sqrt{\left(x_p - \xi_q\right)^2 + \left(y_p - \eta_q\right)^2} + J_{imp} \quad (4)$$

where subscripts p and q refer to different subsections, $p = 1, \cdots, N$ and $q = 1, \cdots, N$. Complex equations in (5) of a single subsection may be written to a matrix equation of the whole cross-section, as shown in Equation (5).

$$(\mathbf{U} + j\mathbf{G})\mathbf{J} = \mathbf{K} \quad (5)$$

8

in which $\mathbf{U}$ is an identity matrix, $\mathbf{J}$ is a column matrix of current densities, $\mathbf{K}$ represents a constant matrix with all elements equalling J_{imp}, and $\mathbf{G}$ is given by Equation (6).

$$\mathbf{G} = \frac{\omega \mu \sigma}{2\pi} a_s{}^2 \log \mathbf{D} \tag{6}$$

where $\mathbf{D}$ contains distances between the center of square subsections. After establishing $\mathbf{D}$ for the cross-section, $\mathbf{J}$ is solved by matrix inversion. R_{ac} of the conductor is then calculated based on conservation of dissipated power in the whole cross-section and in N subsections. A MATLAB script was developed to create a general distance matrix $\mathbf{D}$ adapted to arbitrary polygonal cross-sections, then construct the matrix equation in Equation (6), and finally to solve for R_{ac} per unit length of the SS316 samples. Analytical results show good agreement with FE approximations for the four cross-sectional shapes from 10 Hz to 300 kHz, giving differences within 1%.

Results

Case 1: Plain Geometry Non-magnetic Samples of Varying Cross-sectional Shape

Except for the nominal simulation path of Path-0.8, another path called Path-4.2 which is near the center of surfaces was created on the SS316 models. FE results of PDs measured from the two paths, i.e. close to and far from the edges, are shown in Figure 7. The circular model gives almost identical PDs of two paths in the whole frequency range, reaching 0.22 mV at 300 kHz with 2 mm distances. On other models with polygonal cross-sections, PDs of Path-0.8 are higher than those of Path-4.2. Such differences increase with the frequency, and moreover, as the cross-sectional shape varies from circular to triangular. PDs measured from two paths on the triangular model reach 0.39 mV and 0.14 mV at 300 kHz, resulting in a difference of 179% (based on the lower value). With regard to comparisons between the cross-sectional shapes, PDs obtain from the two uniform paths on different models display clear differences. By sampling the frequency to 300 kHz, the largest difference, which is observed between PDs of Path-0.8 given by the circular and triangular models, is 77%. Nevertheless, experimental results of PD do not exhibit significant differences between the samples, as shown in Figure 8.

Comparisons of PDs for the SS316 samples/models of the four cross-sectional shapes are presented in Figure 9, including experimental results after the data processing, analytical solutions, the nominal FE approximations, and error bars. Analytical solutions of PD were simply calculated by multiplying R_{ac} that was solved from the theory of current integration equation by the total current of 3 A. The calculation assumes uniform current distributions inside and outside the samples, thereby, only offers rough estimations of PD. As the cross-sectional shape changes from circular to triangular, analytical solutions slightly increase and eventually become higher than PDs of Path-4.2 for the triangular shape.

By comparing between experimental and the nominal FE results, good agreement is achieved for the triangular and square samples, with experimental results consistently located inside error bars for the whole frequency range. While for the hexagonal and circular samples, limited fitness are obtained from contrasts between experimental and FE results. Error bars I of measurement locations vary significantly among four cross-sectional shapes. On the circular model, error bars I show small differences to the nominal
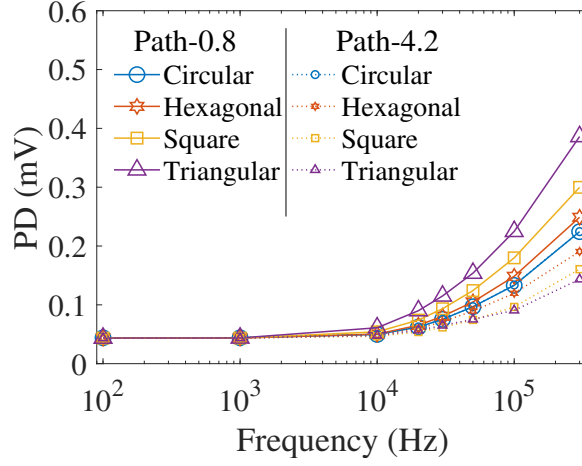
Figure 7: FE results of PD on Path-0.8 (close to the edges) and Path-4.2 (far from the edges) approximated by the PS SS316 models.
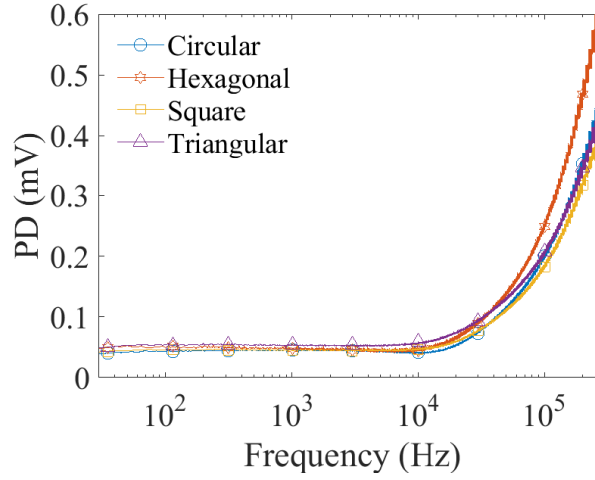

Figure 8: Experimental results of PD measured from the uniform positions in 2 mm on the plain SS316 samples in Case 1.

results on Path-0.8 within 0.6%. The sizes of error bars I increase as the shape approaches to triangular, resulting in the maximum differences of 17% to the nominal results at 300 kHz on the triangular model. Error bars II of measurement distances are uniform regardless of the cross-sectional shape and frequency, which gives constant differences to the nominal results of -25% to 50%.

It will be discussed later that the differences in FE results of PD between models are attributed to current concentration around edges of varying degrees on different cross-sectional shapes, i.e. current crowding. The findings in Case 1 indicate that the measuring methods currently used in the experiments are incapable of identifying current crowding in the SS316 samples with the dimension of 100 mm^2. This motivates the use of ferro-magnetic conductors of EN1A in subsequent experiments. Since the skin effect on the surface of EN1A samples is pronounced and significantly greater than the current crowd-ing, the current distributions on surface is dominated by skin effect and hardly affected by current crowding. Therefore, surface measurements on EN1A samples in the ACPD experiments are less sensitive to measurement uncertainties (especially in locations).
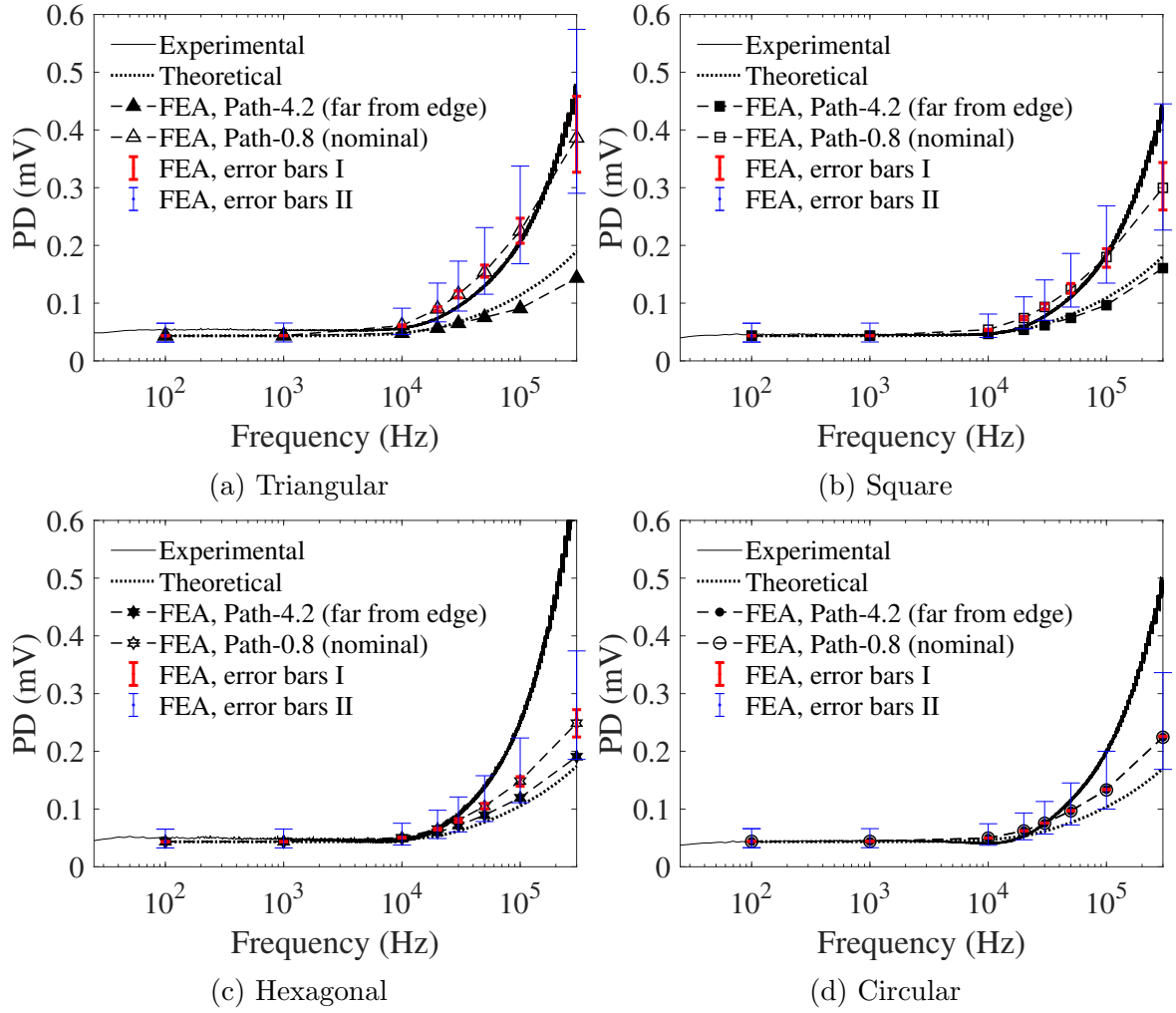
10

Figure 9: Results of PD on the uniform measurement path obtained through various methods for the plain SS316 samples in Case 1.

Case 2: Featured Magnetic Samples (H, N6, NH)

Considering the significant skin effect induced in EN1A conductors, the swept frequencies were sampled from 10 Hz to 50 kHz in experiments of Cases 2 & 3, which gave δ from 0.3 mm to 4.8 μm in EN1A. As shown in Figure10, experimental results of PDs obtained in Case 2 exhibit clear differences. PDs measured across the N6 and NH features are similar and significantly higher than results for the H feature, reaching 1.08, 1.02, and 0.41 mV for 2 mm distances at 50 kHz, respectively.

Comparison of experimental and FE results of PD for the samples in Case 2 are demonstrated in Figure 11. For all the three features, experimental PDs show good agreement with the nominal approximations measured from Path-0.8 and are located inside error bars. Error bars I & II in regards to the three features demonstrate clear differences in sizes. The N6 model produces the minimum error bars I which causes differences smaller than $\pm 10\%$ to the nominal results of Path-0.8. Error bars I given by the H and NH models are similar that the negative parts have small sizes while the positive parts increase significantly with the frequency. At the highest achievable frequency (in FEA) of 10 kHz, the positive parts of error bars I (given by Path-1.1) on the H and NH models lead to differences of 40% higher than the nominal results. For error bars II, those
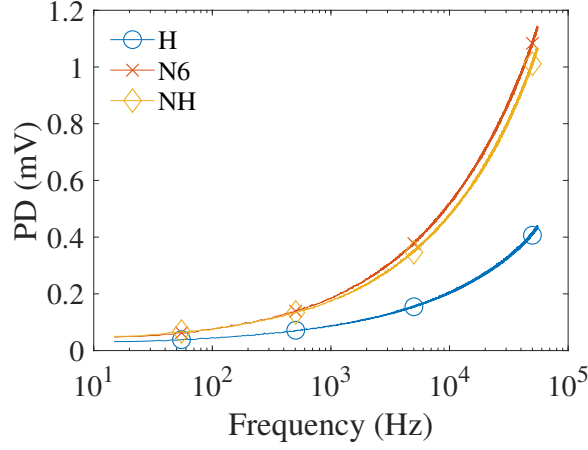
11

Figure 10: Experimental results of PD measured from the uniform points in 2 mm on the square EN1A samples containing the H, N6, and NH features in Case 2.

given by the N6 and NH models are almost constant for the whole frequency range and bring in differences in PDs of -10% to 20%. Whereas, on the H model, error bars II are significant and raise gradually with the frequency, leading to differences of -35% to 60% g to the nominal results at 10 kHz.

Case 3: Featured Magnetic Samples with Varying Features of the Constant Cross-sectional Area (N6, N3, N1.5)

As shown in Figure 12, despite of the same cross-sectional area shared by the N6, N3, and N1.5 features, experimental results of PD measured across the three features display significant differences. At 50 kHz, PDs across the N1.5 and the N3 feature in 2 mm distances reach 0.47 mV and 0.72 mV, respectively.

In comparisons shown in Figure 13, experimental results agree well with the nominal approximations of Path-0.8 for both two features. Moreover, discrepancies between two types of results are completely covered by error bars. Error bars I on the N3 model have limited sizes that are ±15% different to the nominal results. Similar to the H and NH models, error bars I approximated by the N3 model have small negative parts and significant positive parts which raise with the frequency and lead to differences of 40% in PDs at 10 kHz. By comparing with results of the N6 model in Figure 11b, the sizes of error bars II increase as the feature becomes narrower from the N6 towards N1.5. The maximum error bars II on the N1.5 model produce differences of -30% to 60%.

Discussion and Conclusions

Identification for Cross-sectional Shapes of Plain Samples

As shown in Figure 7, the differences of PDs between two measurement locations (Path-0.8 and Path-4.2) and four cross-sectional shapes of models indicate non-uniform distributions of current on the surfaces, and moreover, various impact on current distributions caused by different cross-sectional shapes. Approximated current fields of the four cross-sectional shapes with frequency of 100 kHz are shown as examples in Figure 14. Path-0.8 and Path-4.2 are marked out with black lines. The current field on the circular model
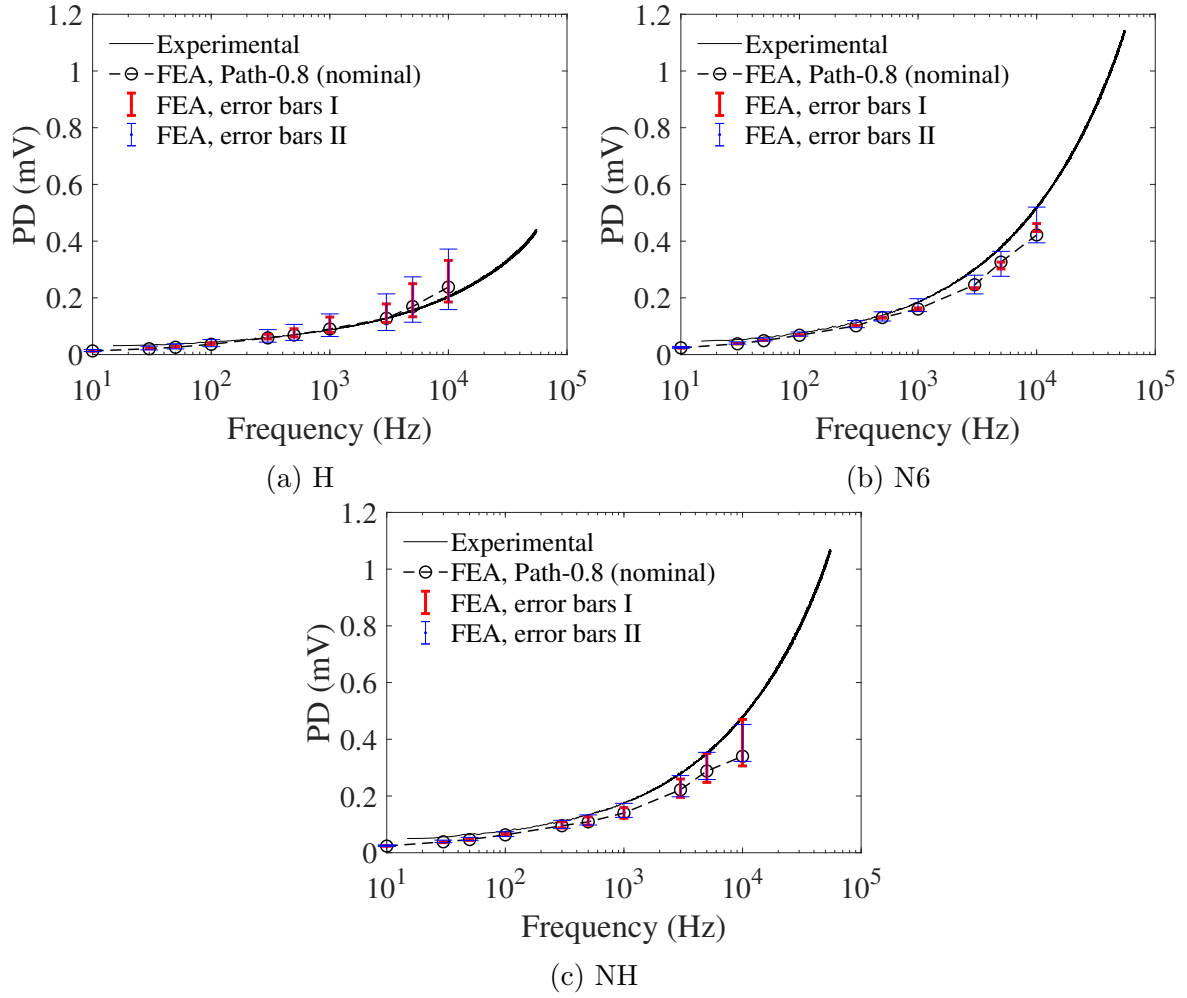
(a) H

(b) N6

(c) NH

Figure 11: Results of PD on the uniform measurement path obtained through various methods for the square EN1A samples in Case 2.
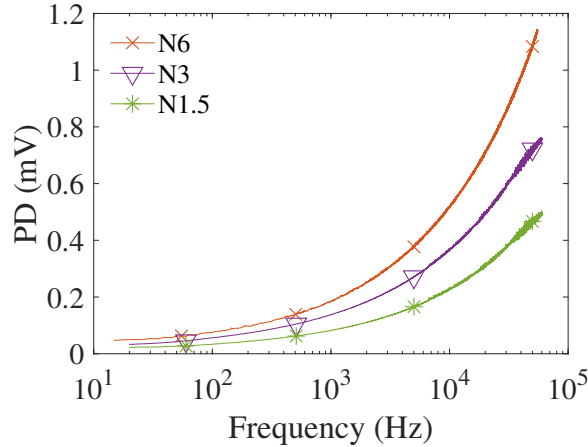

Figure 12: Experimental results of PDs measured from the uniform points in 2 mm on the square EN1A samples containing the N6, N3, and N1.5 features in Case 3.

is uniform on the surface, resulting in identical PDs of two paths (0.22 mV) and negligible error bars I smaller than 0.6%. On the other models, the current is consistently concentrated near the sample edges. The concentrations at the edges become more pro-
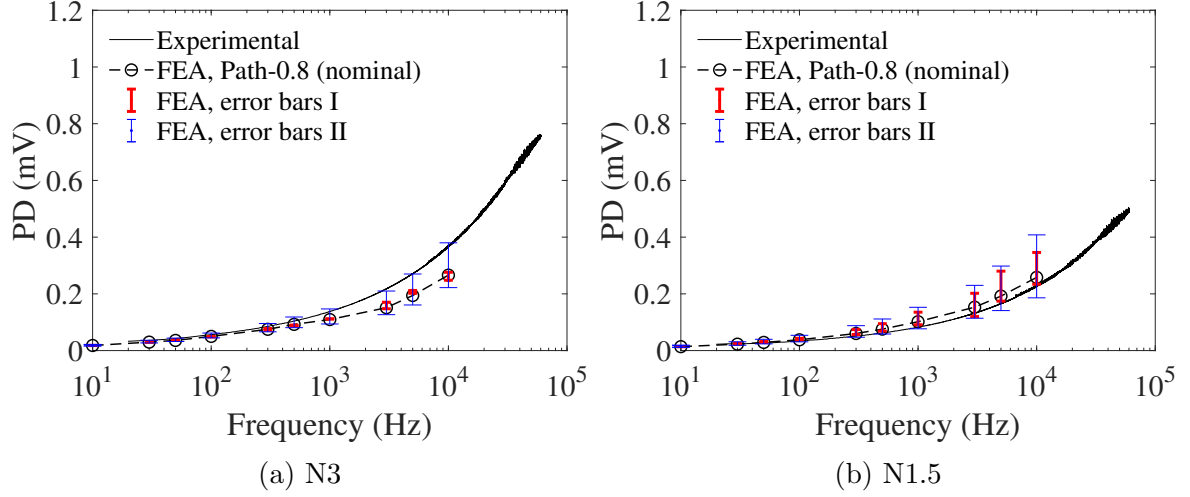
(a) N3 (b) N1.5

Figure 13: Results of PD on the uniform measurement path obtained through various methods for the square EN1A samples in Case 3.

nounced as the polygonal cross-sectional shape varies from quasi-circular to triangular, which is known as the current crowding accompanying with the skin effect at high frequencies [39, 40]. The triangular model offers the largest gaps between PDs of two paths of 179% (0.39 mV and 0.14 mV) and the maximum error bars I which reaches 17% at 300 kHz. Since the analytical solutions of PD were calculated by ignoring skin effect within and outside the samples, these solutions are supposed to be smaller than experimental and FE results that were measured on the surfaces with the maximum current density due to skin effect. This conclusion is observed for the circular and hexagonal shapes with no or weak current crowding in Figures 9c-9d. However, for the triangular and square shapes in Figures 9a-9b, analytical solutions are higher than PDs of Path-4.2, which suggests that the current crowding at edges are prominent and even disturb the skin effect on surface center.

Based on above discussions, the method of measuring swept ACPD signals from uniform positions close to the edges are anticipated to be able to distinguish between the various cross-sectional shapes of non/weak-magnetic conducts like SS316 in which the current crowding are prominent on surfaces. For the SS316 samples with the cross-sectional area of 100 mm^2, the maximum difference in ACPD results between the circular and triangular sample at 300 kHz are of 77%. The similar results of experimental PDs of different cross-sectional shapes and the limited agreement between experimental and FE results for the circular and hexagonal shapes are assumed to be due to measurement uncertainties. Since the cross-sectional shapes are constant and the current excitations are assumed to be longitudinal at the center of samples, any uncertainties in vertical measurement distances result in proportional errors in results of PDs. It is shown by the consistent error bars II giving -25% to 50% of differences in PDs on all models at all frequencies. This is due to the constant variations in measurement distances, i.e. -25% shorter and 50% longer than the nominal distance of 2 mm. For example, a small uncertainty of 0.5 mm in the vertical position of each probe (i.e. 3 mm in the total measurement distance) causes a significant margin of error of 50% in PDs. It is believed that the welding uncertainties actually occurred in experiments were larger than the values covered by error bars I & II.
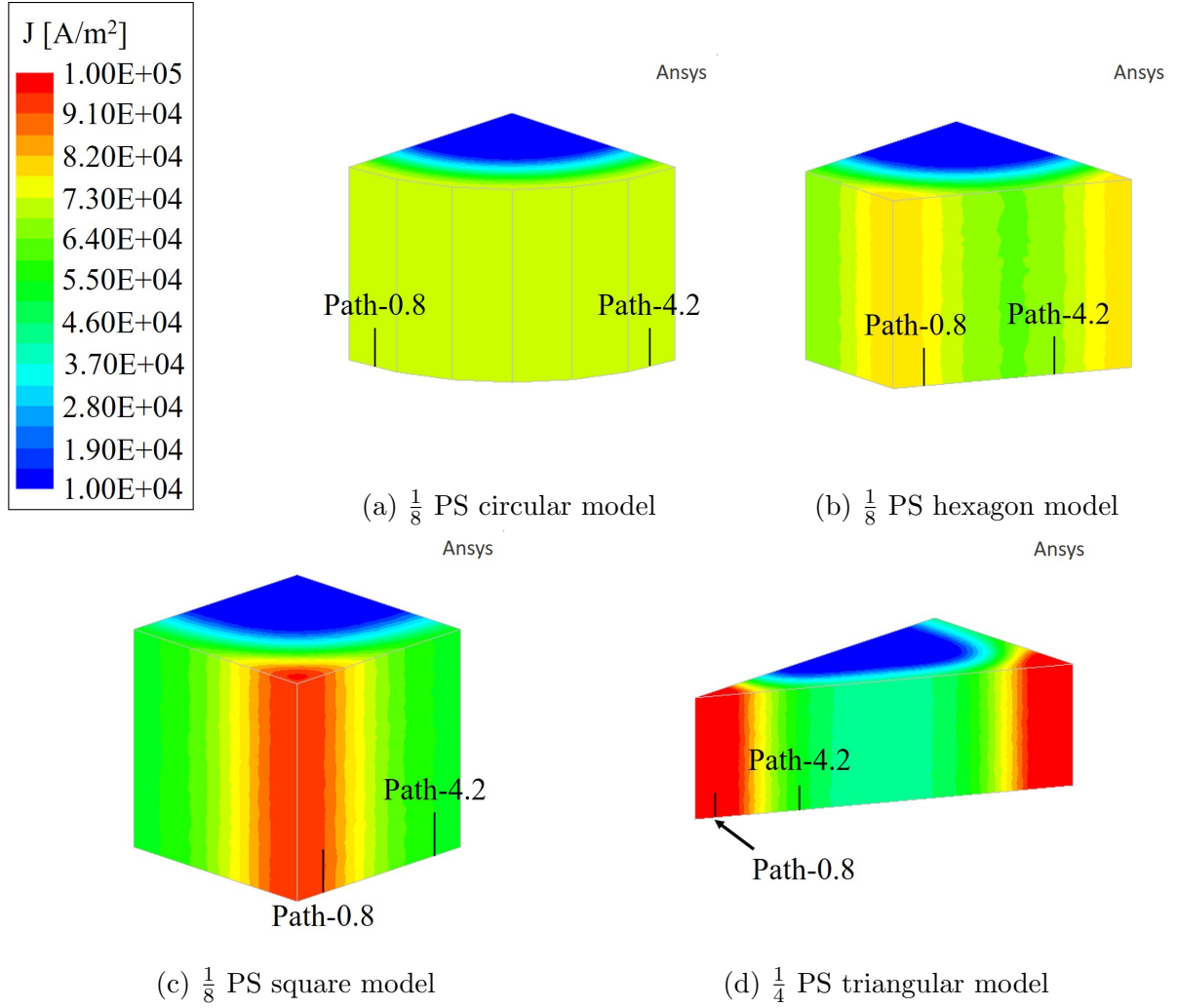
14

Figure 14: FE approximations of the current fields approximated by the PS SS316 models at 100 kHz.

(a) $\frac{1}{8}$ PS circular model

(b) $\frac{1}{8}$ PS hexagon model

(c) $\frac{1}{8}$ PS square model

(d) $\frac{1}{4}$ PS triangular model

Detection for Features in Featured Samples

FE approximations of current fields around the five features with frequency at 1 kHz are shown in Figure 15. Path-0.8, -0.5, and -1.1 are marked out. Currents are consistently concentrated at the feature roots and more uniform (also less distributed) around the sample corners. The roots of the H and N1.5 features are located at 1.06 mm to the edges and close to the conductive paths. While on the N3 and N6 models, the feature roots at 2.12 mm and 4.24 mm are far from the paths. Therefore, measurements within the observation region (from 0.5 mm to 1.1 mm to the edges) on the H and N1.5 models are greatly affected by the non-uniform fields around the roots and thus produce significant error bars I & II. Especially Path-1.1 on the two models, Path-1.1 are beyond the feature roots at 1.06 mm and pass through the current concentration areas on the surfaces near the roots, which gives rise to significant positive parts of error bars I.

In Figure 15, the features influence the current distributions in the vicinity of them. The current around features are not restricted to skin depth as beneath the plain surfaces but penetrate into the depth of features to varying degrees. The electric fields along Path-0.8 across five features are shown in Figure 16 to demonstrate various disturbances in fields caused by different features. The fields are displayed against distances rather than
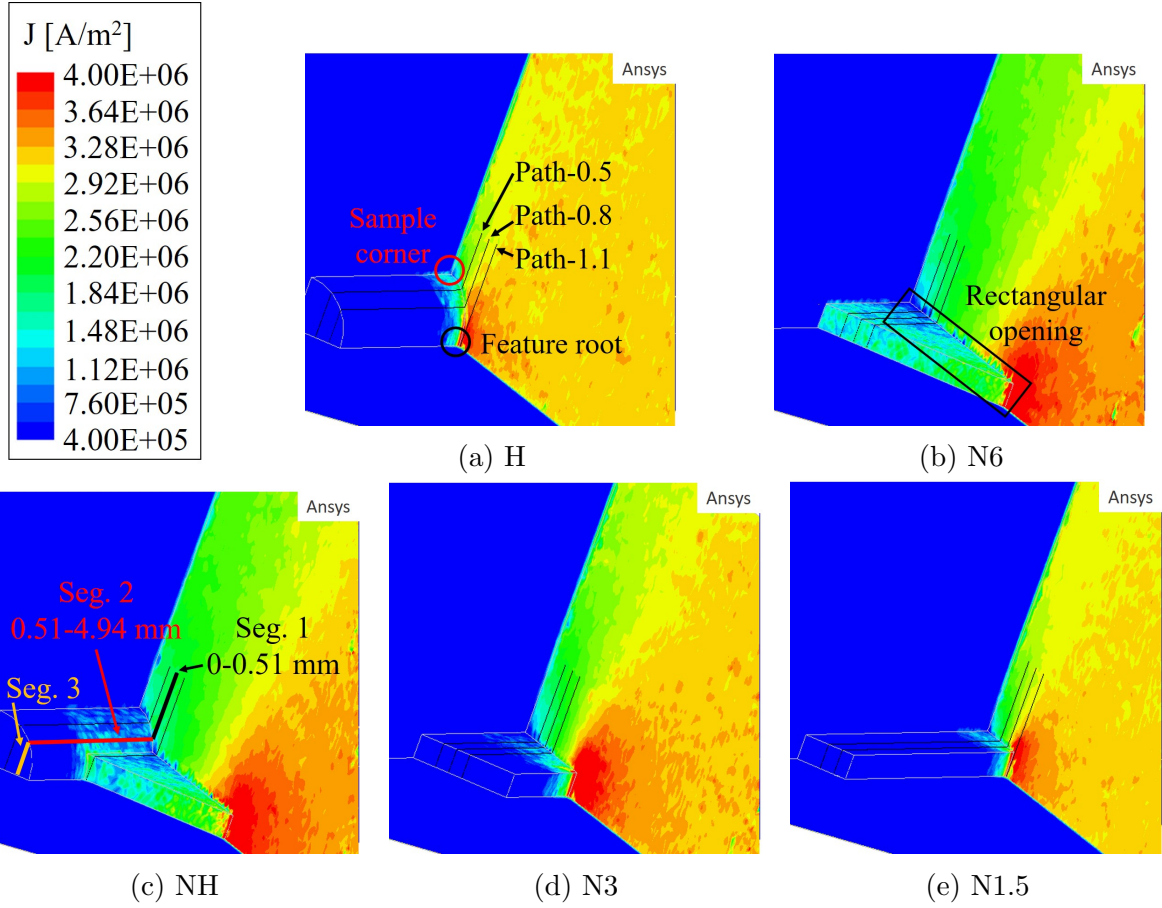
Figure 15: FE approximations of the currents fields approximated by the PS EN1A models at 1 kHz.

the vertical displacement of 1.5 mm, with origins located at the ends farthest to the sample center. The junctions of three line segments of Path-0.8 are indicated in the axis (e.g. see in Figure 15c for three segments across the NH feature). In Figure 16, the fields on two narrow features of H and N1.5 rapidly decrease to 0 around 3 mm, suggesting that the current are highly concentrated on the sample surfaces and vanished within shallow depths around the openings of the features. On the contrary, the fields on the N6 feature, which has the widest opening, do not decline but vary about 0.02 V/m for the whole distance. This indicates that the current around the N6 feature is distributed on all surfaces outside and inside and cover the complete length of Path-0.8. In other words, the narrow features cause limited disturbance in the current distributions so that the current around the feature openings is strongly governed by the skin effect; while the wide features greatly affect the skin effect and thus the current flows on the inside surfaces even reaches the innermost faces of the features. Such differences enable the ACPD methods to differentiate between the the H and N6 features which have dissimilar opening shapes. By comparing the NH feature with the H, the existence of the N6 feature brings in more current distributions on the curved surface, which can be seen in field plotting in Figures 15a & 15c. Additionally, the electric fields along the second segment from 0.51-0.94 mm on the NH feature are higher than those of the H feature, as shown in Figure 16a. The total PD of Path-0.8 across the NH feature is dominated by effect of the N6 feature, whereas the H feature causes minor effect on the current distribution

16

but leads to higher sensitivity to measurement uncertainties. Then contrasting between results of the features in Case 3, as the features openings become narrower, i.e. towards the N1.5, the penetration depths of the current around the openings clearly decrease (in Figures 15b, 15d-15e) and the fields vanish more rapidly with the distances (in Figure 16b).
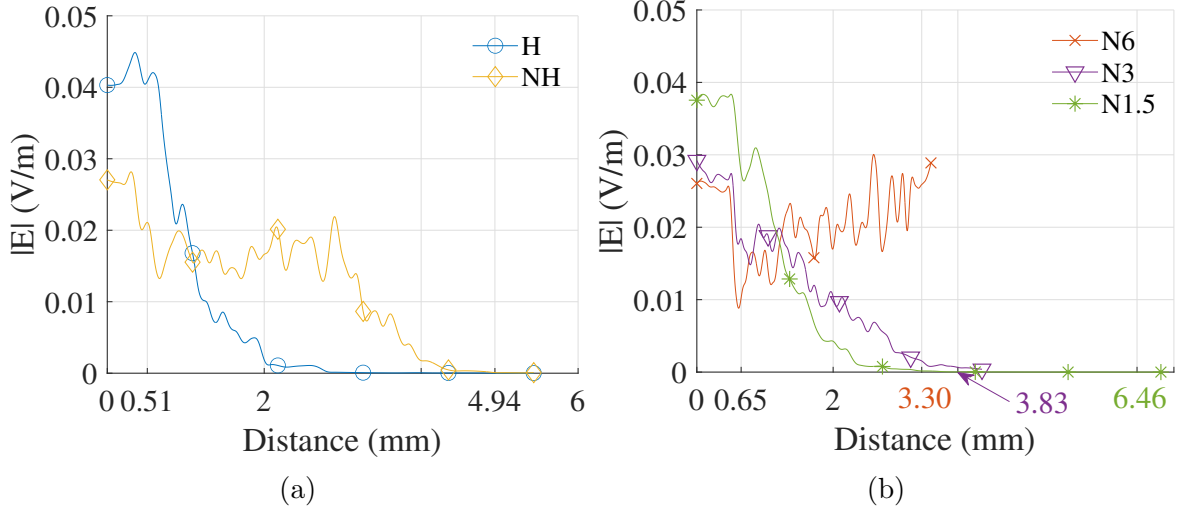

Figure 16: FE approximation of the electric fields on Path-0.8 in the same PS EN1A models at 1 kHz.

Consequently, the swept frequency ACPD method is capable of identifying the features with different opening shapes even have the same cross-sectional area as in the Case 3. This is due to that different opening shapes (i.e. widths) bring in various influence to the current distributions, and hence lead to different penetration depths of the current on the inside features surfaces. Such differences can be identified by ACPD results measured from the uniform positions. Experimental results of PD measured at the uniform positions close to the edges across N6, N3, and N1.5, which have different opening widths of 11%, 21%, and 42% to the sample size, reach 0.47, 0.72, and 1.08 mV of 2 mm distances at 50 kHz, respectively. Nevertheless, in detection of narrow and deep features inside ferromagnetic materials, the current distributions around the features are nearly determined by the skin effect and hence hardly penetrate into the sample. Hence the detection of inner situations in the depth of the features is restricted by insufficient information of little current distributions. The detection capability is highly sensitive to measurement uncertainties, experimental equipments and measurements with high fidelity are required. It was observed that PDs measured from a single path contain too few information to depict the whole geometry of a feature. To further approximate the complete shape of the feature, it was suggested to measure several PDs from multiple locations across and near to the feature.

References

[1] R. Ritchie, *Crack growth monitoring: some considerations on the electrical potential method.* Cambridge Univ., Department of Metallurgy and Materials Science, 1972.

17

[2] D. Sidey, *The measurement of crack growth in metals by the electrical potential method.* Univ., Engineering Department, 1973.

[3] R. Smith, "Calibrations for the electrical potential method of crack growth measurement by a direct electrical analogy," *Strain*, vol. 10, no. 4, pp. 183–187, 1974.

[4] R. Smith and A. Cameron, "A three dimensional wax analogue for the calibration of the electrical potential technique of crack growth monitoring," in *Fracture 84*. Elsevier, 1984, pp. 3371–3376.

[5] G. Klintworth and G. Webster, "Optimization of electrical-potential methods of measuring crack growth," *The Journal of Strain Analysis for Engineering Design*, vol. 14, no. 4, pp. 187–192, 1979.

[6] N. Tada, M. Uchida, A. Funakoshi, and H. Ishikawa, "Experimental study of three-dimensional identification of semi-elliptical crack on the back surface by means of direct-current electrical potential difference method of multiple-point measurement type," *Journal of pressure vessel technology*, vol. 133, no. 1, 2011.

[7] K. Tarnowski, D. Dean, K. Nikbin, and C. Davies, "Predicting the influence of strain on crack length measurements performed using the potential drop method," *Engineering Fracture Mechanics*, vol. 182, pp. 635–657, 2017.

[8] M. Hicks and A. Pickard, "A comparison of theoretical and experimental methods of calibrating the electrical potential drop technique for crack length determination," *International Journal of Fracture*, vol. 20, no. 2, pp. 91–101, 1982.

[9] W. Soboyejo, R. Reed, and J. Knott, "On the calibration of the direct current potential difference method for the determination of semi-elliptical crack lengths," *International journal of fracture*, vol. 44, no. 1, pp. 27–41, 1990.

[10] H. Johnson and A. Willner, "Moisture and stable crack growth in a high strength steel," *Applied Materials Research*, vol. 4, no. 1, pp. 35–40, 1965.

[11] P. McIntyre and A. Priest, "Measurement of sub-critical flaw growth in stress corrosion, cyclic loading and high temperature creep by the dc electrical resistance technique," Tech. Rep., 1971.

[12] E. Santos-Leal and R. J. Lopez, "Simultaneous measurement of acoustic emission and electrical resistance variation in stress-corrosion cracking," *Measurement Science and Technology*, vol. 6, no. 2, p. 188, 1995.

[13] N. Merah, T. Bui-Quoc, and M. Bernard, "Calibration of dc potential technique using an optical image processing system in lcf testing," *Journal of testing and evaluation*, vol. 23, no. 3, pp. 160–167, 1995.

[14] N. Merah, "Dc potential drop calibration in creep-fatigue loading conditions," *Journal of testing and evaluation*, vol. 28, no. 4, pp. 301–306, 2000.

[15] S. Na, D. Yoon, J. Kim, H. Kim, and D. Kim, "An evaluation of the fatigue crack propagation rate for powder metallurgical nickel-based superalloys using the dcpd method at elevated temperatures," *International Journal of Fatigue*, vol. 101, pp. 27–35, 2017.

[16] H. Johnson, "Calibrating the electric potential method for studying slow crack growth," *Materials Research and Standards*, vol. 5, no. 1, pp. 442–445, 1965.

[17] G. Clark and J. Knott, "Measurement of fatigue cracks in notched specimens by means of theoretical electrical potential calibrations," *Journal of the Mechanics and Physics of Solids*, vol. 23, no. 4-5, pp. 265–276, 1975.

[18] J. Knott, "The use of analogue and mapping techniques with particular reference to detection of short cracks," in *The Measurement of Crack Length and Shape During Fracture and Fatigue[Proc. Conf.], Birmingham, England, May 1979,*, 1980, pp. 113–135.

[19] L. Doremus, Y. Nadot, G. Henaff, C. Mary, and S. Pierret, "Calibration of the potential drop method for monitoring small crack growth from surface anomalies–crack front marking technique and finite element simulations," *International Journal of Fatigue*, vol. 70, pp. 178–185, 2015.

[20] A. Campagnolo, G. Meneghetti, F. Berto, and K. Tanaka, "Calibration of the potential drop method by means of electric fe analyses and experimental validation for a range of crack shapes," *Fatigue & Fracture of Engineering Materials & Structures*, vol. 41, no. 11, pp. 2272–2287, 2018.

[21] Y. Si, J. Rouse, and C. Hyde, "Potential difference methods for measuring crack growth: A review," *International Journal of Fatigue*, vol. 136, p. 105624, 2020.

[22] E. C. Jordan, *Electromagnetic waves and radiating systems / Edward C. Jordan, Keith G. Balmain.*, 2nd ed., ser. Prentice-Hall electrical engineering series. Englewood Cliffs, N.J.: Prentice-Hall, 1968.

[23] I. S. Grant and W. R. Phillips, *Electromagnetism.* John Wiley & Sons, 2013.

[24] T. Venkatsubramanian and B. Unvala, "An ac potential drop system for monitoring crack length," *Journal of physics E: scientific instruments*, vol. 17, no. 9, pp. 765–771, 1984.

[25] Y. Nakai and R. Wei, "Measurement of short crack lengths by an ac potential method," *Engineering fracture mechanics*, vol. 32, no. 4, pp. 581–589, 1989.

[26] I. Hwang, "A multi-frequency ac potential drop technique for the detection of small cracks," *Measurement Science and Technology*, vol. 3, no. 1, pp. 62–74, 1992.

[27] S. Tiku, N. J. Marchand, and B. Unvala, "An advanced multiple frequency acpd system for crack detection and calibration," in *Nontraditional methods of sensing stress, strain, and damage in materials and structures.* ASTM International, 1997.

[28] H. Saguy and D. Rittel, "Alternating current flow in internally flawed conductors: A tomographic analysis," *Applied physics letters*, vol. 89, no. 9, p. 094102, 2006.

[29] G. Sposito, P. Cawley, and P. B. Nagy, "An approximate model for three-dimensional alternating current potential drop analyses using a commercial finite element code," *NDT & E International*, vol. 43, no. 2, pp. 134–140, 2010.

[30] Y. Li, F. Gan, Z. Wan, J. Liao, and W. Li, "Novel method for sizing metallic bottom crack depth using multi-frequency alternating current potential drop technique," *Measurement Science Review*, vol. 15, no. 5, p. 268, 2015.

[31] T. M. Buss, "Advanced techniques for the estimation of crack shape and detection of crack growth in mechanical tests," Ph.D. dissertation, University of Nottingham, 2023.

[32] S. Ramo, J. R. Whinnery, and T. Van Duzer, *Fields and waves in communication electronics.* John Wiley & Sons, 2008.

[33] M. A. Heald and J. B. Marion, *Classical electromagnetic radiation.* Courier Corporation, 2012.

[34] M. S. Raven, "Experimental measurements of the skin effect and internal inductance at low frequencies," *Acta Technica*, vol. 60, no. 1, 2015.

[35] P. Silvester, "Modal network theory of skin effect in flat conductors," *Proceedings of the IEEE*, vol. 54, no. 9, pp. 1147–1151, 1966.

[36] P. Silvester, *Modern Electromagnetic Fields*, ser. Microwaves and fields series. Prentice-Hall, 1968.

[37] G. Antonini, A. Orlandi, and C. R. Paul, "Internal impedance of conductors of rectangular cross section," *IEEE Transactions on Microwave Theory and Techniques*, vol. 47, no. 7, pp. 979–985, 1999.

[38] A. Rong and A. C. Cangellaris, "Note on the definition and calculation of the per-unit-length internal impedance of a uniform conducting wire," *IEEE transactions on electromagnetic compatibility*, vol. 49, no. 3, pp. 677–681, 2007.

[39] A. Payne. The ac resistance of rectangular conductors. [Online]. Available: https://www.researchgate.net/publication/351307928_THE_AC_RESISTANCE_OF_RECTANGULAR_CONDUCTORS

[40] A. Payne. Skin effect, proximity effect and the resistance of circular and rectangular conductors. [Online]. Available: https://www.researchgate.net/publication/351306996_SKIN_EFFECT_PROXIMITY_EFFECT_AND_THE_RESISTANCE_OF_CIRCULAR_AND_RECTANGULAR_CONDUCTORS